Ultrasonic guided waves interaction with cracks in the front glass of thin-film solar photovoltaic module

Dicky Silitonga [a,*], Nico F. Declercq [a], Pascal Pomarède [a,c], Fodil Meraghni [c], Bertrand Boussert [b], Pooja Dubey [a]

[a] George W. Woodruff School of Mechanical Engineering, Georgia Institute of Technology, GT-Europe, IRL 2958 Georgia Tech – CNRS, 2 rue Marconi, Metz, 57070, France
[b] Electrical and Computer Engineering, Georgia Institute of Technology, GT-Europe, 2 rue Marconi, Metz, 57070, France
[c] Arts et Métiers ParisTech, LEM3 UMR CNRS 7239, 4 rue Augustin Fresnel, Metz, 57078, France

A B S T R A C T

As the solar photovoltaics power system sees rapid growth in installed capacity and plays a significant role in the future global energy mix, its reliability becomes a crucial factor in maintaining the stability of the electricity supply. Manufacturing imperfections and harsh operating environments may compromise the module's structural integrity, leading to performance deterioration and power loss. Therefore, nondestructive inspection becomes an indispensable part of the quality assurance or maintenance program to detect defects at any stage of the module's lifecycle. Ultrasound is an essential method for material inspection, and ultrasonic-guided waves have been long explored as a flaw detection technique on plate-like structures, taking advantage of its long-range detection that yields an efficient inspection process superior to the conventional pulse-echo technique. Inspired by the same idea, this work assesses the prospect of harnessing ultrasonic guided waves, particularly Lamb waves, to detect cracks, as they exist in an actual module. However, unlike the commonly investigated plates, solar photovoltaic modules contain stacks of a-few-microns-thick layers of different materials that add complexities to the structure. The investigated specimen is a thin film photovoltaic module with cracks caused during transportation and handling. It, therefore, represents a real-life research case that may occur in situ. Numerical and experimental methods are performed to reveal various Lamb modes that propagate in the structure, where the results of both methods are mutually confirmed. Unlike other works, this investigation is not confined to the utilization of the non-dispersive mode but attempts to find the defect-sensitive mode that can be used to detect cracks. An analysis of the experimental results reveals the mode most sensitive to cracks, while numerical simulations explain the corresponding phenomena.

1. Introduction

Solar photovoltaics (PV) has grown exponentially as a clean energy source in recent decades [1]. It has been proven a practical solution to generate electricity on various scales, from powering a single electronic appliance to being an alternative means of electricity production in remote locations and a source to supply grid systems. It offers flexibility for installation, be it in a dedicated area such as a solar farm, as an additional building feature, or in any other modes of installation, either fixed or equipped with a solar tracker. This versatility leads to an optimistic projection of the future solar photovoltaics module (SPVM) installation. Commercial SPVM generally falls into silicon crystalline and thin film technology, where the latter currently attracts growing attention due to its low production cost potential [2–4]. Furthermore, there still exist many areas open for improvement in the field of thin film solar cells. Besides the standard silicon-based cells, other thin film technologies with improved efficiency are undergoing progressive development, such as gallium nitride (GaN) cells, passivated emitter and rear contact (PERC), and the III-V semiconductors. Although their efficiency is relatively lower compared to the crystalline type modules, the cost-effectiveness of thin film SPVM due to less material usage becomes one of its major selling points in the market. With continuous innovation in thin film technology that tunes up the efficiency of thin film cells, the demand for this type of SPVM is also expected to grow.

As the contribution of PV power generation increases in the future global energy mix [5], the reliability of PV systems becomes a crucial factor in supporting grid stability. Among the efforts to maintain the reliability of PV systems is structural health monitoring (SHM) of individual SPVM. Mechanical defects in the front glass panel may lead to power loss by obstructing sunlight transmission into the cells or damaging the cells and electrical contacts. In addition, the presence of crack may also serve as a precursor to other kinds of defects as it allows moisture to penetrate the solar cell, leading to delamination, corrosion, broken circuit, discoloration, or short circuit [6]. Therefore, besides keeping a check on the module's structural integrity, the results of the SHM inspection on SPVM are valuable concerning the module's

* Corresponding author.
E-mail addresses: dsilitonga@gatech.edu, djsilitonga@gmail.com (D. Silitonga).

performance deterioration. Electroluminescence (EL) and infrared (IR) thermography have been the widely used methods for SPVM inspection, mainly for finding hotspot, faulty cells and circuitry [7]. Those two methods are effective for cell inspection since their working principles are based on phenomena occurring in the cells, for instance heating (IR) or photons emissions due to carrier recombination (EL). That way, their capability to detect defects on the other module's components outside the electric current path, like the glass, back panel and encapsulant, is limited. Those methods detect cell cracks, yet it may not be able to resolve the overall condition of module's layers. For mechanical defect inspection of the whole structure, ultrasonic technique is more appropriate than the previously mentioned methods because it can detect structural flaws not only in the cells but throughout the module, which includes delamination, air voids and crack [8]. In addition, ultrasonic technique does not require the module to be energized during inspection.

Conventional ultrasonic scanning technique works by sending ultrasonic signal into the material towards its thickness-wise direction and has two kinds of measurement methods: pulse-echo and transmission. In pulse-echo method, the analyzed signal is the echo coming back to the transducer. On the other hand, transmission method observes the signal received by another transducer at the other side of the structure. Ultrasonic C-scan method collects point-by-point measurements over a given area, producing a map of that enables inspector to locate the exact position and determine the characteristics of the defects. It is a mature and proven method to detect micro-scaled flaws in materials as practiced in various fields. Nevertheless, the inspection process with this conventional ultrasonic bulk wave C-scan method is slow since it needs to examine numerous points to generate a high-resolution image. Hence, the technique is impractical for many SPVM-related use cases, such as final inspection on a fast-moving production line or periodic inspection on a large-scale solar PV power plant.

A promising alternative acoustic method to detect mechanical defects in SPVM is by employing ultrasonic guided waves (UGW). In a plate-like structure, UGW travels in the direction parallel to the plane of principal surfaces, guided by the structure's boundaries, as opposed to the bulk waves that propagate in the thickness-wise direction. Unlike the conventional C-scan method that measures in a point-by-point manner as outlined before, this method benefits from UGW's ability to travel a long distance, interrogating greater area at each measurement which reduces inspection time. Investigators have been using this method to detect discontinuities in plates of various materials, including composites [9–11], hence encouraging the authors to adopt the method for inspecting SPVM, which is essentially a multilayered plate that resembles the structure of composites. Nevertheless, an SPVM has a unique structure that differentiates it from other composite materials. In SPVM, multiple thin layers of different materials are sandwiched by substantially thicker plates. Meanwhile, in most laminated plates or composites, the thin layer between two primary plates is a single material, like an adhesive layer. To this end, literature surveys can bring insights since the study of UGW in multilayered plates has been published by many researchers [12–14]. Still, further investigation is necessary to understand the characteristics of UGW in a particular plate constructed with a typical combination of materials and layer thickness, as found in SPVM.

In this paper, we aim to understand the characteristics of UGW in a thin film SPVM with a vision toward its utilization for a non-destructive evaluation technique. Here, our study focuses on how the UGW interacts with cracks as a significant defect that directly affects structural integrity. This investigation combines numerical simulation and experimental methods to describe the propagation characteristics of UGW in the SPVM specimen and the phenomena associated with the interaction of waves with cracks.

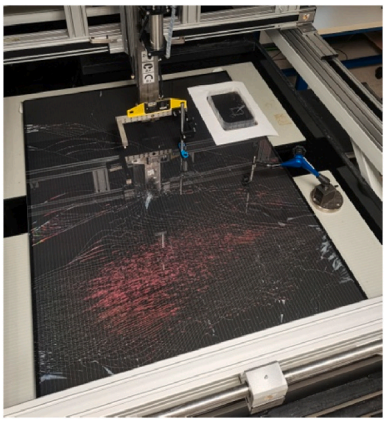

Fig. 1. The solar module specimen under the 5-axis ultrasonic scanner.

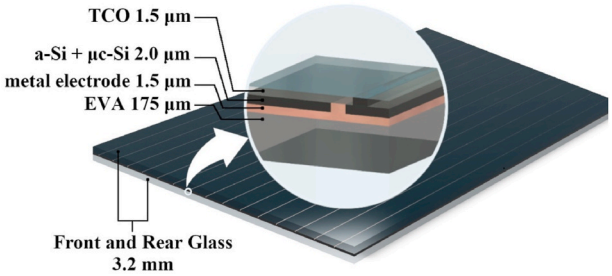

Fig. 2. Anatomy of the module with details of solar cell structure, materials, and thickness. Notice that the metal portion that protrudes into the Si layer are the lines visible from the front side through the TCO (the schematic is drawn according to the information from SHARP Energy Solutions Europe).

2. Sample description

The SPVM investigated in this work is a thin-film type solar cell manufactured by SHARP (model NA-E135-L5). As stated in the product datasheet, this model features a tandem structure of amorphous and microcrystalline silicon layer. Fig. 1 shows the specimen under a 5-axis scanner arm in our laboratory. The specimen is a full-size module measuring 1401 mm × 1001 mm with an overall thickness of 6.58 mm. A closer look from the front side of the module, as depicted in Fig. 2, shows that solar cells are assembled in a stripes-like pattern that runs in the lengthwise orientation of the module. The bright lines visible from the front side, uniformly spaced at 10.5 mm, are portions of rear metal electrodes that protrude through the thin film layer.

The cross-sectional anatomy of the SPVM specimen received from the manufacturer is illustrated in Fig. 2. It is a multilayered structure with glass plates sandwiching the solar cell assembly. Note that the illustration is not to scale since the physical dimension of the solar cell assembly is much thinner than the glasses. Underneath the upper glass is a layer of TCO (transparent conductive oxide) coating, followed by silicon layers and rear metal electrodes. EVA (ethylene vinyl acetate) is an encapsulant to seal the cells, prevent moisture ingress, and bond the back glass to complete the module assembly. The solar cell itself is of a tandem type; thus, the Si part is a micromorph that consists of microcrystalline Silicon (µc-Si) bottom cell and amorphous Silicon (a-Si) top cell.

Our specimen contains defects that occurred due to transportation and handling activities. There are cracks of varying severity and density throughout the front glass plate. In some areas, there is also delamination visible from the front side. Since the defects are caused by real-world activities instead of artificially induced damages, this investigation is expected to deliver results that are more pertinent to the actual

Table 1
Layers specifications of the specimen model for numerical simulations.

Layer	Material	Thickness (mm)	Density (g/cm^3)	Young's modulus (GPa)	Poisson's ratio
1	Glass (Soda lime)	3.2	2.5	73	0.24
2	TCO (FTO)	0.0015	6.8	150	0.33
3	a-Si + μcSi	0.0020	2.3	181	0.22
4	Rear electrode:				
	Cu	0.0015	7.8	110	0.34
	– 0r –				
	Ag	0.0015	10	76	0.37
5	EVA	0.175	0.94	0.02	0.45
6	Glass (Soda lime)	3.2	2.5	73	0.24

operations of the SPVM. However, there exist consequences of these actual defects, i.e., their randomness in shape and size, since they occurred in an uncontrolled manner. Therefore, it is essential to obtain the dimensional detail of defects, in this case, the cracks under scrutiny. This task, presented in the result section of this paper, was accomplished by employing Scanning Acoustic Microscopy (SAM). Cracks were observed through SAM imaging with a 400 MHz transducer that scanned an area where a crack exists at a resolution of 2.5 μm.

3. Numerical simulations of the UGW dispersion in the structure

A model of a multilayered plate was numerically simulated to provide preliminary information on the behavior of UGW prior to experiments and to verify the results of experimental data processing. DISPERSE, a dispersion curves calculator software was employed for this task. The simulated model was a multilayered plate mimicking the structure of the investigated SPVM specimen in terms of materials and thickness of the layup, except that the model is a stack of infinite plates. The infinite character of the model was approached in the experiments by measuring in areas away from edges to alleviate the reception of edge reflection. In addition, all measurements were made in the direction parallel to the visible lines, representing cell assembly patterns, since the received wave was intended to have traveled along a uniformly flat structure. Otherwise, the waves would have encountered a periodic structure of solar cell patterns along their propagation path in a line between transducers.

Although the types of glass, TCO, and rear electrodes are undisclosed by the manufacturer, shortlisted materials commonly used in commercial SPVM can be selected to build the model. The typical solar panel front cover material is soda lime float glass [15]. The actual thickness measurement of our specimen's glass panels is 3.2 mm, consistent with the standard thickness figure of industrial glasses available in the market. As the transparent conductive oxide, FTO (fluorine-doped tin oxide) is the widely chosen material in the market owing to its low-cost [16–18]. For the rear electrode, Cu, Ag, Al, and Mo are some of the suitable metals. When simulating the model with those metals as the rear contact layer, there was no noticeable difference in the Cu, Ag, and Mo dispersion curves. The Al showed different curves where one higher frequency mode deviated off the position of the same mode in other metals' dispersion curves. Of those three possible metal choices, Mo is more favorable in CIGS or perovskite solar cells [19–22]. Meanwhile, our module is based on Si solar cells. Thus, it can be assumed that the metal in our specimen is either Cu or Ag, both being standard materials for Si-based solar cell rear electrodes [23,24]. The simulations showed that selecting any of those two metals as the element of the simulated model does not make any difference in the resulting dispersion curves. Table 1 describes the constituents of the specimen with their corresponding mechanical properties as input values for calculating dispersion curves in DISPERSE.

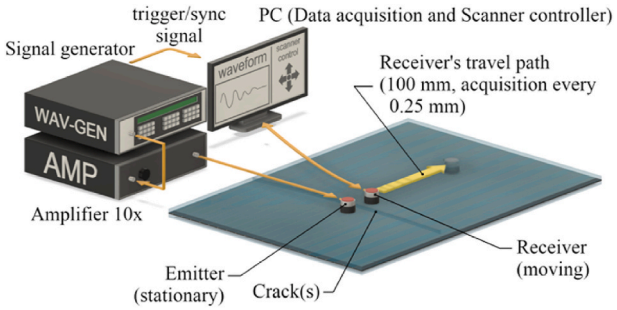

Fig. 3. Schematic of the experimental setup to obtain dispersion curves.

4. Experiment

We studied the characteristics of UGW in SPVM by observing dispersion curves of the modes propagating in the structure. For this purpose, a setup as schematized in Fig. 3 was designed to experiment as Alleyne and Cawley [25]. It allowed the acquisition of signals from a series of equally spaced points which were then processed with a 2D Fourier transform procedure in MATLAB to plot dispersion curves in a frequency-wavenumber space. This setup used two contact transducers: one as a stationary emitter and another as a receiver mounted on a moving scanner arm. The arm of a 5-axis ultrasonic scanner (POLAR C-Scan) carried the receiver along a 100 mm line path while the system recorded a time-domain waveform every 0.25 mm. Thus, every run of the experiment registered waveforms from 400 points. The receiver started at 30 mm from the emitter, and the final distance between transducers at the end of the scanning stroke length was 130 mm.

The emission signal was a 5-burst sinusoidal pulse of 500 kHz frequency, generated by a waveform generator (Stanford Research Systems DS345), which then underwent a 10x amplification before reaching the emitting transducer. Both transducers (Panametrics V103) were of longitudinal wave type, positioned at normal incidence concerning the plane of the plate by placing the transducers' face in contact with the front glass surface. Water was introduced as a couplant on both transducers, considering the practical reason that it is a standard substance for cleaning SPVM, thus ensuring the safety and possibility for future adaptation of the proposed technique to the regular module cleaning activities.

During the experiment, the scanner was set to line scanning mode in the direction parallel to the solar cell strips. This direction was chosen to receive the waves that traveled in a uniformly flat structure between the transducers, undistracted by the solar cell's strip patterns that the waves would bump into should they propagate towards other directions. Therefore, the condition of the received waves in the experiment could approximate that of the infinite flat plate geometry model on the numerical simulation. Measurements were conducted on pristine and cracked areas to study the influence of cracks on the propagation of UGW in SPVM by comparing and analyzing the resulting dispersion curves. Areas with cracks of different severity levels were investigated in this work, as shown in Fig. 4: (b) one crack, (c) two cracks, and (c) a shattered area. In the case of investigating one and two cracks, transducers were placed such that the defect was located in the 30 mm gap between the transducers at the receiver's initial position.

5. Results

The crack image obtained from SAM presented in Fig. 5 shows a line of one-pixel width. Since the resolution of the SAM is limited to 2.5 μm/pixel, the crack can be of any width up to that size and is classified as a microcrack. In the SPVM defect terminology, any cracks less than 30 μm in width are microcracks [26,27]. From visual observation of the specimen, the crack in the investigated areas penetrates through the entire front glass thickness. In contrast, the back panel glass is perfectly intact.

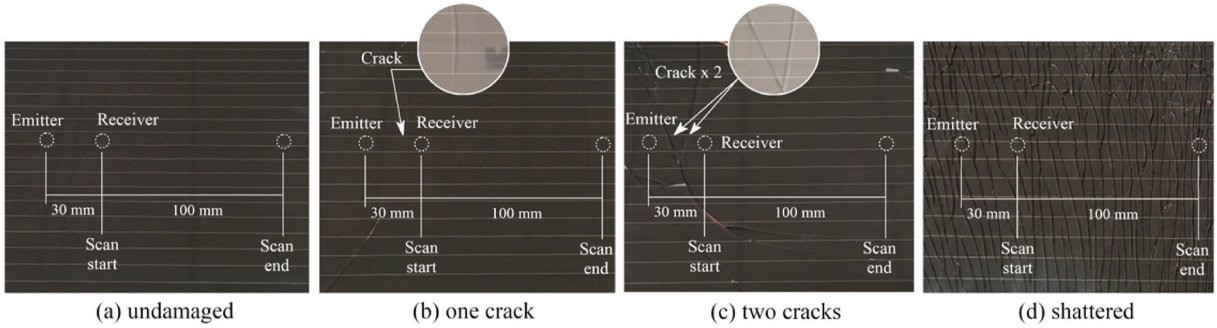

Fig. 4. Conditions investigated in the experiments.

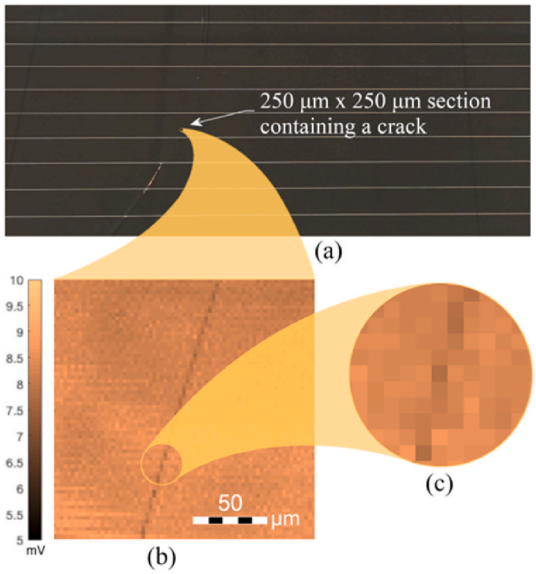

Fig. 5. SAM observation: (a) The section containing a typical crack investigated in this work; (b) SAM image of the crack; (c) Further magnification of the SAM image showing the crack as a line of one-pixel width.

Recalling that our experimental setup involved contact transducers placed on the top glass surface and that the transducers were optimized for longitudinal waves, i.e., perturbation out of the element's plane, the receiver would predominantly pick up vertical displacement of the surface. Therefore, in the experiment, we observed mainly Lamb waves by picking up out-of-plane motion. Accordingly, horizontal shear modes were either weakly probed or undetected in the received signals.

DISPERSE calculation yielded 13 Lamb modes within the range up to 1.5 MHz, plotted in frequency-wavenumber (f-k) and frequency-phase velocity (f-v_{ph}) diagrams in Fig. 6(a) and (b), respectively. Whatever mode is considered, it is not necessarily symmetric or anti-symmetric throughout its spectrum since the plate structure does not form any symmetry [28] in either geometry or material properties. Evidence of this is shown in Fig. 6(c), where mode 1 is symmetric about the horizontal midplane at the low wavenumber region but anti-symmetric at a higher part of the curve, as demonstrated by the numerically simulated shape of plate displacement. This behavior also occurs in other modes, although some retain the shape throughout the curve. Therefore, to designate the modes in Fig. 6, plain numbers from 1 to 13 are assigned without mentioning any symmetric or anti-symmetric characteristic.

There are multiple approaches to selecting the most appropriate mode in Lamb waves inspection techniques. A standard method is by exciting a mode in its non-dispersive frequency range, and another is by selecting a specific mode sensitive to particular defects [29]. By examining the f-v_{ph} curves in Fig. 6(b), it is evident that mode 2 is an excellent choice for the non-dispersive mode excitation method owing to its flat velocity profile over a broad frequency regime. It exhibits an insignificant velocity change (5523 m/s $\pm$ 0.6%) over a broad frequency band between 100 and 400 kHz. Being a lower frequency mode is also an advantage of mode 2, allowing it to travel greater distances. Moreover, by exciting mode 2 in the lower part of its non-dispersive band (100 kHz–200 kHz), the occurrence of mode conversion, if any, will be evident since the only possible converted Lamb mode is unmistakably mode 1. Indeed, selecting and analyzing the first appearing modes at low frequency, or the fundamental modes, are the standard practice in Lamb waves-based inspection technique [30–32].

Although the technique of exciting pure non-dispersive modes is simple and mature, it is, for our purposes, insufficiently sensitive to

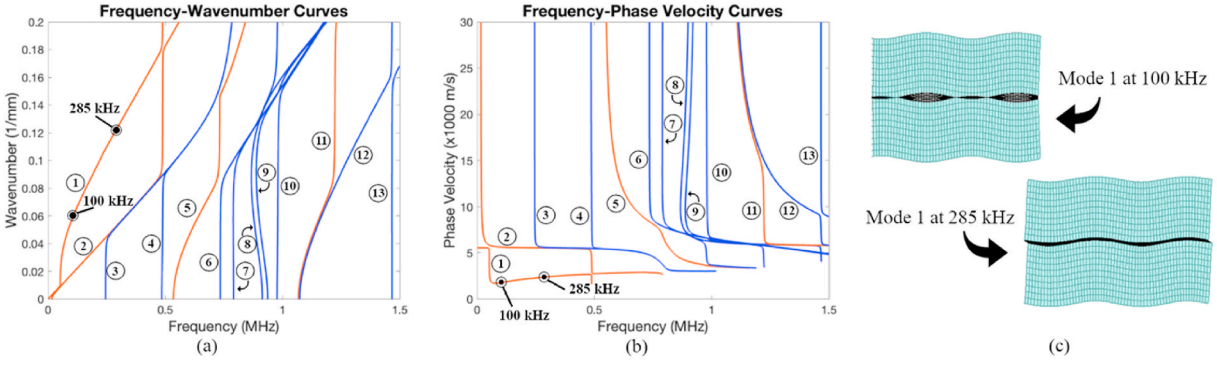

Fig. 6. Plots of dispersion curves generated from DISPERSE simulation: diagrams of frequency versus (a) waveform and (b) phase velocity. The number corresponds to the nearby mode curve, and the red curves are the propagating modes appearing in the experiments. (c) Shapes of mode 1 at 100 kHz and 285 kHz demonstrate different symmetry behaviors within the same mode. (For interpretation of the references to color in this figure legend, the reader is referred to the Web version of this article.)

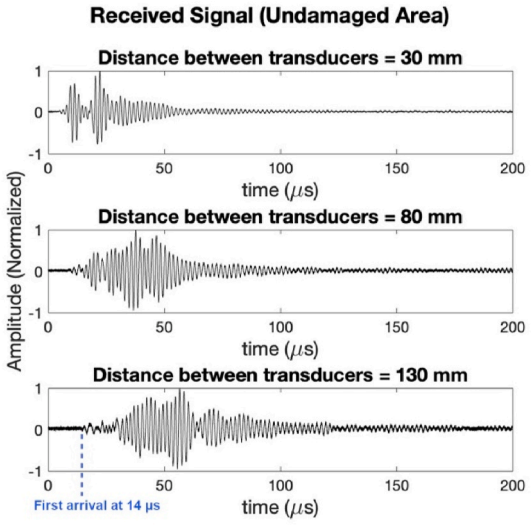

Fig. 7. Waveforms of signals on the undamaged area at three different emitter-receiver distances.

minor defects due to the relatively long wavelength of the low frequency these fundamental modes have. This shortcoming is known and becomes the reason why researchers have explored techniques that exploit other, more sensitive modes [33,34], to detect microcracks in materials like metals and composites, although this far has not been explored in SPVM research.

When such modes are used, a non-dispersive nature is no longer the primordial focus but rather the selection of modes that appear to undergo substantial changes upon interaction with certain defects. Thus, any mode may be suitable, offering a wide range of frequency and wavelength choices. On the other hand, while selecting the non-dispersive modes requires a relatively straightforward analysis of the dispersion curves, discovering the damage-sensitive modes necessitates an extended effort. In this work, the approach to finding the sensitive modes was carried out experimentally. The modes of interest are those with sensitivity to cracks, under the focus of this paper, as stated in the introductory section.

Dispersive nature of the propagating UGW in the SPVM specimen can be discerned from the change in time signal waveform shape at different distances, as depicted in Fig. 7. It shows the waveforms of UGW signals obtained experimentally from three distances between the emitter and receiver in the undamaged area. The amplitude is normalized to

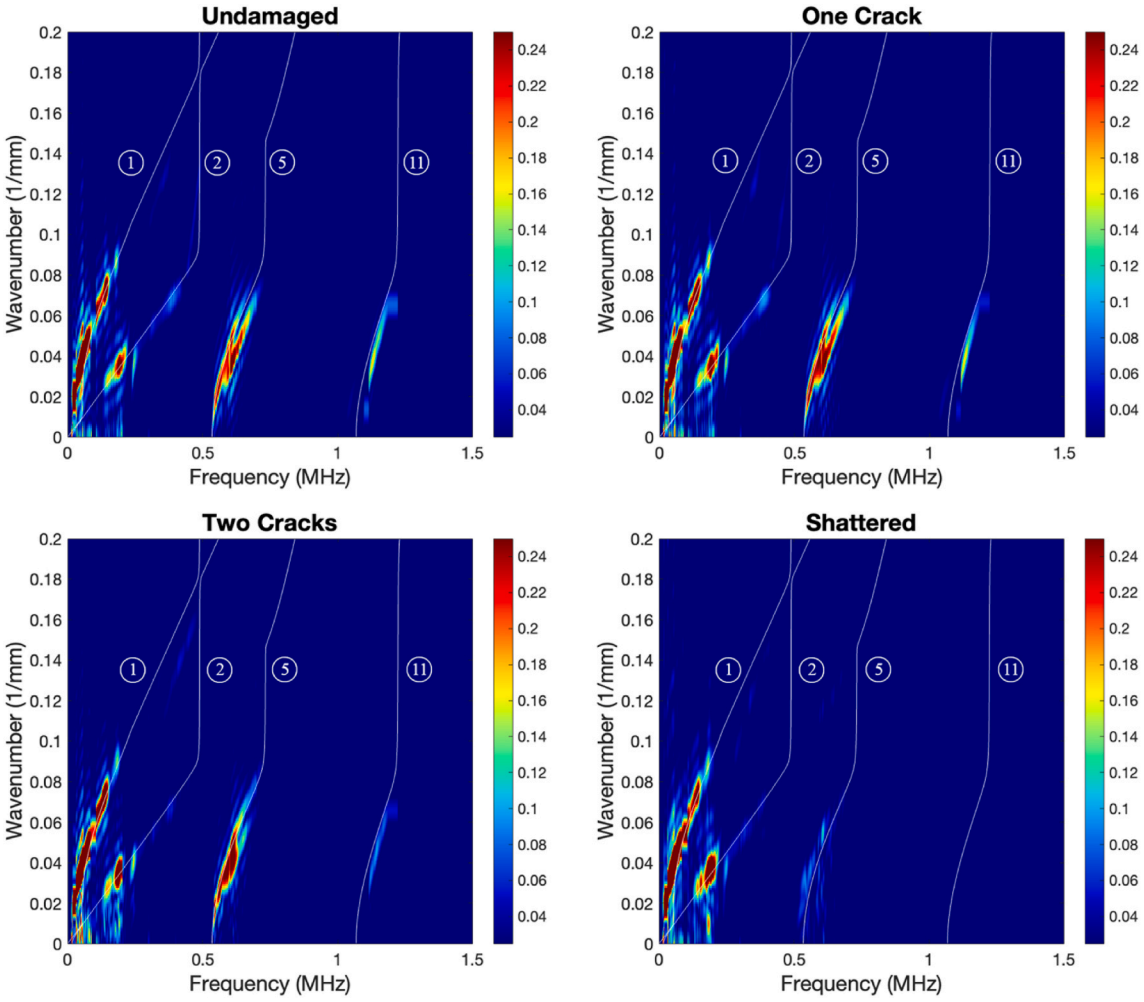

Fig. 8. Dispersion curves of Lamb waves obtained from experiments on 4 areas with different conditions (refer to Fig. 4). Out of 13 theoretical modes according to DISPERSE simulation within 0–1.5 MHz range, four modes appear: modes 1, 2, 5, and 11. Although the dispersion curves obtained from the undamaged area (top left) and the area with one crack (top right) look similar, the color trace along Mode 11 is slightly weaker in the area with crack, indicating the decrease in the mode's intensity. When the guided waves travel through two cracks, color trace along Mode 11 noticeably fades out, implying further suppression in its intensity (bottom left). In the shattered area (bottom right), Mode 11 is no longer visible in the diagram and even the intensity of Mode 5 is significantly reduced. (For interpretation of the references to color in this figure legend, the reader is referred to the Web version of this article.)

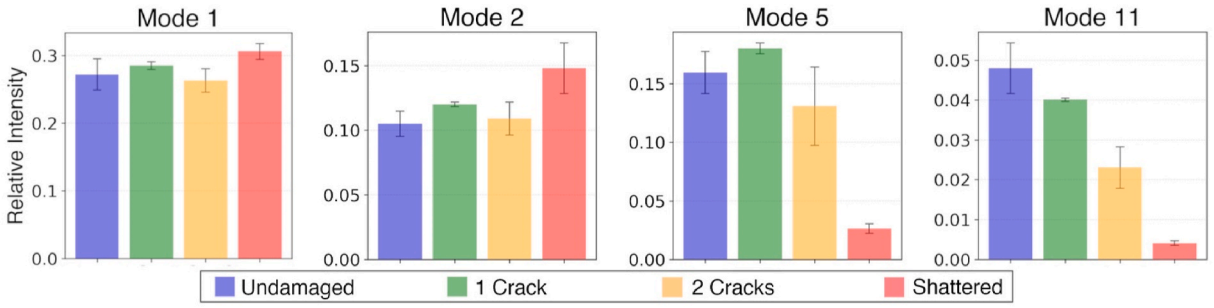

Fig. 9. The relative intensity of the bright areas in Fig. 8, in the range of $k = 0.03$ mm^{-1} to $k = 0.05$ mm^{-1}, for mode 1 (30 kHz–80 kHz), mode 2 (150 kHz–200 kHz), mode 5 (580 kHz–630 kHz), and mode 11 (1100 kHz–1160 kHz). Error bars indicate standard errors from 3 experiments. Mode 11 demonstrates consistent intensity reduction with increased crack severity in the solar module's front panel.

emphasize the evolution of the waveform shape over the propagation distance due to the dispersive nature of UGW. At the emitter-receiver distance of 130 mm, the first arrival of the signal appears at 14 μs, which yields 9290 m/s of wave velocity. As the discussion proceeds, it will be shown that this velocity is within the range of the velocity of the fastest propagating mode in the specimen during the experiments. That mode lies in a higher frequency band beyond the fundamental modes.

The experimental dispersion curves were plotted as a color-scaled diagram in MATLAB by performing a 2-D Fourier transform to the time-space matrix of waveforms acquired from a series of positions. Four diagrams of dispersion curves from the measurements on areas with different conditions are presented in Fig. 8. To enable comparison with simulation results, the curves generated by DISPERSE software are overlaid on the diagrams. Those diagrams demonstrate that there are 4 Lamb wave modes excited in the experiments, as indicated by the high-intensity color traces, which coincide with 4 of the curves in Fig. 6(a): mode 1, mode 2, mode 5, and mode 11. The non-visible modes are either non-existent or considerably less dominant relative to the appearing modes, which can be related to the perpendicular angle of incidence of the emission signal. Changing the angle of incidence by placing the transducers in an oblique orientation will shift the dominance of and generate the invisible modes in the present experiments [33,35,36]. However, our work stayed as close as possible to real applications in which normal incidence is expected. Therefore, despite the absence of some theoretical modes, the plots in Fig. 8 still indicate that numerical results agree with the experimental counterparts, hence validating the methods employed in this work.

The color plots in Fig. 8 show modes 1 and 2 consistently appearing in all cases, regardless of damage severity, inferring their insensitivity to crack types assessed in this investigation. The plots also demonstrate that the defects do not induce any mode conversion in all modes throughout the spectrum. In contrast to the first two modes, modes 5 and 11 exhibits characteristic behavior as their intensity diminishes with increasing damage severity, with mode 11 being the most impacted. To quantitatively present this observation, the mean of pixel values in the high-intensity areas in Fig. 8 are calculated and plotted as bar charts in Fig. 9. The mean value is taken to represent the level of intensity strength around a select area. One can compare mode intensities at different cracking conditions by inspecting the charts. The areas in Fig. 8 considered for the calculations are rectangles bounded vertically from wavenumber (k) 0.03/mm to 0.05/mm for all modes; and horizontally within the frequency (f) range of 30 kHz–80 kHz for mode 1, 150 kHz–200 kHz for mode 2, 580 kHz–630 kHz for mode 5, and 1100 kHz–1160 kHz for mode 11. Among those modes, mode 11 shows a consistent decline in intensity as the crack severity escalates.

Common sense may lead to an argument that a higher frequency wave has a shorter wavelength which is indeed more sensitive to discontinuity. Nevertheless, due to the dispersive nature of Lamb waves, the wavelengths of higher-order modes are not necessarily shorter than that of the lower-order modes because the velocities vary throughout their frequency spectra. To prove that argument, a physical example can be taken from the frequency and velocity relation of the first arrived signal, as discussed earlier in Fig. 7. Among the four propagating modes, the relatively high velocity of 9290 m/s found in Fig. 7 at 130 mm emitter-receiver distance is only possible in mode 11 at 1.2 MHz, see Fig. 6(b). With that velocity and frequency pair, the calculated wavelength is 7.7 mm, which is within the wavelength range of mode 5, a mode which lies in the frequency regime far below mode 11, see Table 2. The wavelength of each propagating mode in Table 2 is calculated by selecting the frequency range with a high-intensity color trace in Fig. 8. Then, the value of phase velocity at those selected frequency ranges is extracted from Fig. 6(b). The wavelength is calculated through the relation $\lambda = v_{ph}/f$.

Table 2
Acoustic parameters of the propagating Lamb modes.

Mode	f (kHz)	v_p (m/s)	λ (mm)
1	20–200	2147–5538	10.7–277
2	125–250	5545–5597	22.2–44.8
5	530–700	5032–5443	7.2–10.3
11	1100–1200	6300–29000	5.7–24.2

Despite being within a similar wavelength range, modes 5 and 11 have distinct characteristics regarding their propagation mechanism. Those modes have a different profile of power flow distribution that affects their sensitivity to defects on the plate layers. DISPERSE simulation results, exhibited in Fig. 10, reveal that most waves' energy is located at the lower layer in mode 5. Meanwhile, the opposite profile prevails in mode 11. Likewise, in terms of particle displacement in the direction normal to the surface, i.e., the motion to be probed by the contact transducer, mode 5 creates more dominant displacement in the lower portion of the structure. At the same time, the reverse applies to mode 11.

All the cracks in our specimen exist in the upper glass, or the module's front panel, with the rear glass perfectly intact. Thus, in the case of mode 11, a more significant portion of the wave energy passes through the defective upper glass, scattered and attenuated, diminishing the transmitted energy at the other side of the defect. The portion of the wave energy that propagates in the lower glass, although being undisturbed by defects, only carries a low intensity. Therefore, even if the mode wave can reconstruct downstream of the crack, the wave's overall energy intensity picked up by the receiver is substantially reduced. In addition, the middle layers contain soft EVA polymer with high acoustic absorption, suppressing energy exchange between the lower and upper parts of the structure. Eventually, discontinuities in the upper part of the structure, or the front glass panel of our investigated specimen, are more impactful to mode 11. Therefore, analyzing the behavior of this mode is appropriate for detecting front panel cracks, which is one of the critical failure modes in SPVM operations. From the practical point of view, utilizing this mode is also advantageous because the measurement is

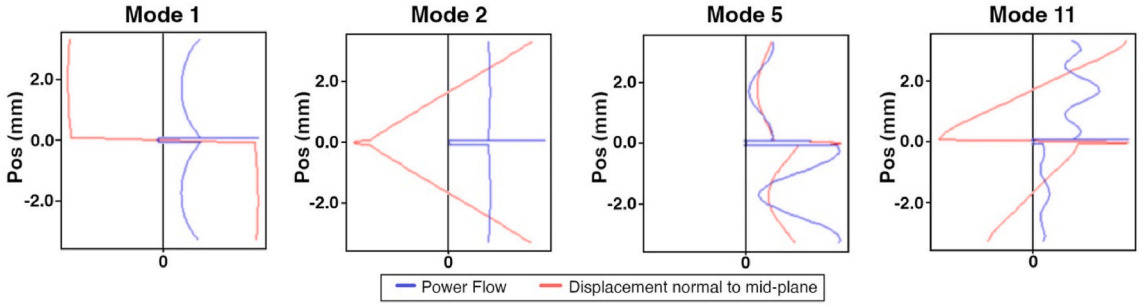

Fig. 10. Power flow distribution and particle displacement normal to surface plane, at wavenumber $k = 0.04$ mm^{-1}. The vertical axis defines the thickness-wise position in the structure (midplane = 0.0, top glass surface = 3.2, bottom glass surface = −3.2), horizontal axis defines the normalized magnitude of each parameter.

made on the front side, where accessibility will not become an issue.

6. Conclusion

This work demonstrates the selection of damage-sensitive Lamb mode to detect cracks in the front glass of SPVM. Experiments were carried out to extract dispersion curves, and the results agree with numerical simulations. This has validated the capability of the experimental technique based on the 2D Fourier transform to capture the propagating modes in a structure with multilayers of micron-thickness films as in SPVM. It is beneficial from the perspective of nondestructive evaluation since the technique is based on an experimental approach familiar with NDT of plate structures in general and applied to SPVM. This method can be embedded in automated mechanisms or module-cleaning devices in prospective practical implementations.

The identification of damage-sensitive modes involved analysis of the intensity of modes as they interact with defects of different severity levels. Results show that a mode undergoes remarkable intensity decay when the waves propagate through areas with increasing cracks. Therefore, that mode can be exploited as a damage indicator to detect cracks and gain information on their severity. Unlike the standard approach of Lamb waves-based inspection that utilizes the low-frequency fundamental modes, the selected damage-sensitive mode is located at the higher frequency band at 1.1 MHz–1.2 MHz.

CRediT authorship contribution statement

Dicky Silitonga: Writing – original draft, Visualization, Methodology, Investigation, Conceptualization. **Nico F. Declercq:** Writing – review & editing, Supervision. **Pascal Pomarède:** Software, Methodology. **Fodil Meraghni:** Writing – review & editing. **Bertrand Boussert:** Writing – review & editing. **Pooja Dubey:** Investigation.

Declaration of competing interest

The authors declare that they have no known competing financial interests or personal relationships that could have appeared to influence the work reported in this paper.

Data availability

Data will be made available on request.

Acknowledgement

The authors appreciate the contribution of SHARP Energy Solutions Europe for providing valuable information regarding product details.

References

[1] Solar PV – Analysis, IEA. (n.d.). https://www.iea.org/reports/solar-pv (accessed August 16, 2022).
[2] G.A. Thopil, C.E. Sachse, J. Lalk, M.S. Thopil, Techno-economic performance comparison of crystalline and thin film PV panels under varying meteorological conditions: a high solar resource southern hemisphere case, Appl, Energy 275 (2020), 115041, https://doi.org/10.1016/j.apenergy.2020.115041.
[3] C.-Y. Tsai, C.-Y. Tsai, Tandem amorphous/microcrystalline silicon thin-film solar modules: developments of novel technologies, Sol. Energy 170 (2018) 419–429, https://doi.org/10.1016/j.solener.2018.05.060.
[4] S. Pouladi, C. Favela, W. Wang, M. Moradnia, N.-I. Kim, S. Shervin, J. Chen, S. Sharma, G. Yang, M.-C. Nguyen, R. Choi, J. Kim, A. Fedorenko, B. Bogner, J. Bao, S.M. Hubbard, V. Selvamanickam, J.-H. Ryou, Significant improvement of conversion efficiency by passivation of low-angle grain boundaries in flexible low-cost single-crystal-like GaAs thin-film solar cells directly deposited on metal tape, Sol. Energy Mater, Sol. Cell. 243 (2022), 111791, https://doi.org/10.1016/j.solmat.2022.111791.
[5] IRENA, Future of Solar Photovoltaic: Deployment, Investment, Technology, Grid Integration and Socio-Economic Aspects (A Global Energy Transformation: Paper), International Renewable Energy Agency, Abu Dhabi, 2019. https://www.irena.org/-/media/Files/IRENA/Agency/Publication/2019/Nov/IRENA_Future_of_Solar_PV_2019.pdf. (Accessed 16 August 2022).
[6] M.A. Munoz, M.C. Alonso-García, N. Vela, F. Chenlo, Early degradation of silicon PV modules and guaranty conditions, Sol. Energy 85 (2011) 2264–2274, https://doi.org/10.1016/j.solener.2011.06.011.
[7] G. Balasubramani, V. Thangavelu, M. Chinnusamy, U. Subramaniam, S. Padmanaban, L. Mihet-Popa, Infrared thermography based defects testing of solar photovoltaic panel with fuzzy rule-based evaluation, Energies 13 (2020) 1343, https://doi.org/10.3390/en13061343.
[8] S.R. Madeti, S.N. Singh, A comprehensive study on different types of faults and detection techniques for solar photovoltaic system, Sol, Energy 158 (2017) 161–185, https://doi.org/10.1016/j.solener.2017.08.069.
[9] D.N. Alleyne, P. Cawley, The interaction of Lamb waves with defects, IEEE Trans. Ultrason. Ferroelectr. Freq, Control 39 (1992) 381–397, https://doi.org/10.1109/58.143172.
[10] J.S. Hall, P. McKeon, L. Satyanarayan, J.E. Michaels, N.F. Declercq, Y.H. Berthelot, Minimum variance guided wave imaging in a quasi-isotropic composite plate, Smart Mater. Struct. 20 (2011), 025013, https://doi.org/10.1088/0964-1726/20/2/025013.
[11] M. Castaings, D. Singh, P. Viot, Sizing of impact damages in composite materials using ultrasonic guided waves, NDT E Int. 46 (2012) 22–31, https://doi.org/10.1016/j.ndteint.2011.10.002.
[12] J.L. Rose, A. Pilarski, J.J. Ditri, An approach to guided wave mode selection for inspection of laminated plate, J. Reinforc. Plast. Compos. 12 (1993) 536–544, https://doi.org/10.1177/073168449301200504.
[13] F. Ricci, E. Monaco, N.D. Boffa, L. Maio, V. Memmolo, Guided waves for structural health monitoring in composites: a review and implementation strategies, Prog. Aero. Sci. 129 (2022), 100790, https://doi.org/10.1016/j.paerosci.2021.100790.
[14] H. Cunfu, L. Hongye, L. Zenghua, W. Bin, The propagation of coupled Lamb waves in multilayered arbitrary anisotropic composite laminates,, J. Sound Vib. 332 (2013) 7243–7256, https://doi.org/10.1016/j.jsv.2013.08.035.
[15] B.L. Allsopp, R. Orman, S.R. Johnson, I. Baistow, G. Sanderson, P. Sundberg, C. Stålhandske, L. Grund, A. Andersson, J. Booth, P.A. Bingham, S. Karlsson, Towards improved cover glasses for photovoltaic devices, Prog. Photovoltaics Res. Appl. 28 (2020) 1187–1206, https://doi.org/10.1002/pip.3334.
[16] A. Way, J. Luke, A.D. Evans, Z. Li, J.-S. Kim, J.R. Durrant, H.K. Hin Lee, W.C. Tsoi, Fluorine doped tin oxide as an alternative of indium tin oxide for bottom electrode of semi-transparent organic photovoltaic devices, AIP Adv. 9 (2019), 085220, https://doi.org/10.1063/1.5104333.
[17] A.-L. Anderson, S. Chen, L. Romero, I. Top, R. Binions, Thin films for advanced glazing applications, Buildings 6 (2016) 37, https://doi.org/10.3390/buildings6030037.
[18] N.P. Klochko, K.S. Klepikova, V.R. Kopach, I.I. Tyukhov, V.V. Starikov, D. S. Sofronov, I.V. Khrypunova, D.O. Zhadan, S.I. Petrushenko, S.V. Dukarov, V. M. Lyubov, M.V. Kirichenko, A.L. Khrypunova, Development of semi-transparent

ZnO/FTO solar thermoelectric nanogenerator for energy efficient glazing, Sol. Energy 184 (2019) 230–239, https://doi.org/10.1016/j.solener.2019.04.002.
[19] W. Li, X. Yan, W.-L. Xu, J. Long, A.G. Aberle, S. Venkataraj, Efficiency improvement of CIGS solar cells by a modified rear contact, Sol. Energy 157 (2017) 486–495, https://doi.org/10.1016/j.solener.2017.08.054.
[20] H. Abdy, A. Aletayeb, M. Kolahdouz, E.A. Soleimani, Investigation of metal-nickel oxide contacts used for perovskite solar cell, AIP Adv. 9 (2019), 015216, https://doi.org/10.1063/1.5063475.
[21] F. Behrouznejad, S. Shahbazi, N. Taghavinia, H.-P. Wu, E.W.-G. Diau, A study on utilizing different metals as the back contact of CH3NH3PbI3 perovskite solar cells,, J. Mater. Chem. 4 (2016) 13488–13498, https://doi.org/10.1039/C6TA05938D.
[22] B. Salhi, The photovoltaic cell based on CIGS: principles and technologies,, Materials 15 (2022) 1908, https://doi.org/10.3390/ma15051908.
[23] L. Tous, R. Russell, J. Das, R. Labie, M. Ngamo, J. Horzel, H. Philipsen, J. Sniekers, K. Vandermissen, L. van den Brekel, T. Janssens, M. Aleman, D.H. van Dorp, J. Poortmans, R. Mertens, Large area copper plated silicon solar cell exceeding 19.5% efficiency, Energy Proc. 21 (2012) 58–65, https://doi.org/10.1016/j.egypro.2012.05.008.
[24] A. ur Rehman, S.H. Lee, Crystalline silicon solar cells with nickel/copper contacts, Intech (2015), https://doi.org/10.5772/59008.
[25] D. Alleyne, P. Cawley, A two-dimensional Fourier transform method for the measurement of propagating multimode signals,, J. Acoust. Soc. Am. 89 (1991) 1159–1168, https://doi.org/10.1121/1.400530.
[26] M.K. da Silva, M.S. Gul, H. Chaudhry, Review on the sources of power loss in monofacial and bifacial photovoltaic technologies, Energies 14 (2021) 7935, https://doi.org/10.3390/en14237935.
[27] Y. Chiou, J. Liu, Y. Liang, Micro crack detection of multi-crystalline silicon solar wafer using machine vision techniques, Sens. Rev. 31 (2011) 154–165, https://doi.org/10.1108/02602281111110013.
[28] V.Y. Zhang, B. Dubus, B. Collet, M. Destrade, Piezoacoustic wave spectra using improved surface impedance matrix: application to high impedance-contrast layered plates, J. Acoust. Soc. Am. 123 (2008) 1972–1982, https://doi.org/10.1121/1.2836756.
[29] D.N. Alleyne, P. Cawley, Optimization of lamb wave inspection techniques, NDT E Int. 25 (1992) 11–22, https://doi.org/10.1016/0963-8695(92)90003-Y.
[30] M.J.S. Lowe, O. Diligent, Low-frequency reflection characteristics of the s0 Lamb wave from a rectangular notch in a plate, J. Acoust. Soc. Am. 111 (2002) 12.
[31] M.J.S. Lowe, P. Cawley, J.-Y. Kao, O. Diligent, The low frequency reflection characteristics of the fundamental antisymmetric Lamb wave a0 from a rectangular notch in a plate,, J. Acoust. Soc. Am. 112 (2002) 12.
[32] T. Wandowski, P.H. Malinowski, W.M. Ostachowicz, Circular sensing networks for guided waves based structural health monitoring, Mech, Syst. Signal Process 66–67 (2016) 248–267, https://doi.org/10.1016/j.ymssp.2015.05.001.
[33] D. Cirtautas, V. Samaitis, L. Mažeika, R. Raišutis, E. Žukauskas, Selection of Higher Order Lamb Wave Mode for Assessment of Pipeline Corrosion, 2022, p. 20.
[34] L. Satyarnarayan, J. Chandrasekaran, B. Maxfield, K. Balasubramaniam, Circumferential higher order guided wave modes for the detection and sizing of cracks and pinholes in pipe support regions, NDT E Int. 41 (2008) 32–43, https://doi.org/10.1016/j.ndteint.2007.07.004.
[35] S.-J. Park, Y.-S. Joo, H.-W. Kim, S.-K. Kim, Selective generation of lamb wave modes in a finite-width plate by angle-beam excitation method, Sensors 20 (2020) 3868, https://doi.org/10.3390/s20143868.
[36] W. Xue, W. Gao, W. Liu, H. Zhang, R. Guo, Impact of Wedge Parameters on Ultrasonic Lamb Wave Liquid-Level Sensor, 2022, p. 13.